Available online at www.sciencedirect.com

SciVerse ScienceDirect

Acta Materialia 60 (2012) 3524–3535

Acta MATERIALIA

www.elsevier.com/locate/actamat

Correlation of particle impact conditions with bonding, nanocrystal formation and mechanical properties in kinetic sprayed nickel

Gyuyeol Bae [a], Jae-il Jang [b], Changhee Lee [a,*]

[a] Kinetic Spray Coating Laboratory, Division of Materials Science and Engineering, Hanyang University, 17 Haengdang-dong, Seongdong-gu, Seoul 133-791, Republic of Korea

[b] Division of Materials Science and Engineering, Hanyang University, 17 Haengdang-dong, Seongdong-gu, Seoul 133-791, Republic of Korea

Received 20 December 2011; received in revised form 8 February 2012; accepted 1 March 2012

Abstract

Owing to the specific high-strain-rate thermomechanical characteristics of Ni particle impact in kinetic spraying, the rebound phenomenon of the impacting particles hinders the formation of the first layer and impedes successful build-up of the coating. Even at higher impact velocities, the deposition efficiency of the coating is quite low because of excessive kinetic energy, which induces the rebound and/or erosion of the highly flattened particles. This paper reports noticeably improved bonding and deposition characteristics of Ni particles resulting from suppressed equivalent (von Mises) flow stress and enhanced interface heat-up as a result of powder preheating. Experimental observations coupled with finite-element modeling (FEM) corroborate the fact that the thermally softened Ni particle is very effective for enhanced adhesive and cohesive bonding. Based on the FEM results, the thermal boost-up zone, increased by thermally accelerated adiabatic shear instability, is proposed as a crucial factor for enhancing bonding between the particles, which is essential in producing better coating properties. Moreover, nanocrystal formation (<100 nm) in the coating was more pronounced than cases previously reported in the literature, mainly because of the enhanced thermal activation and straining of the severely deformed particles, which was verified by transmission electron microscopy investigations and nanoindentation tests.

Keywords: Kinetic (or cold) spray; Nickel; Bonding; Finite-element modeling; Nanocrystal

1. Introduction

Kinetic spraying or cold gas dynamic spraying is a novel technique in which strain-induced adiabatic heating, accompanied by shear instability, enables the formation of interface bonding and coating build-up via high velocity (300–1200 m s^{-1}) impacts of micron-sized particles (typically 1–50 μm) onto a substrate or previously deposited layer [1–4]. Material-specific physico-mechanical properties and high-strain-rate thermo-mechanical characteristics are responsible for the critical velocity required for successful bonding [1–4]. Different aspects of adiabatic shear instability (ASI) in metallic materials have been approximated phenomenologically in terms of a thermal boost-up zone (TBZ) (as depicted in Fig. 1). The TBZ (Z_{tb}) is expressed mathematically by the following equation [3]:

$$Z_{tb} = H_{tb} \cdot W_{tb} = [(T_{max} - T_r)/T_m] \cdot [(t_c - t_i)/t_c] \quad (1)$$

where T_{max} is the maximum temperature, T_r is the temperature of transition point, T_m is the melting temperature (in kelvin), t_i is the incubation time, and t_c is the total contact time, as illustrated in Fig. 1. The multiplication value of H_{tb} and W_{tb} (i.e., Z_{tb} according to Eq. (1)) can be a theoretical criterion which determines the bonding features and properties of kinetic sprayed coatings (e.g., see Ref. [4]).

* Corresponding author. Tel.: +82 2 2220 0388; fax: +82 2 2299 0389.
E-mail address: chlee@hanyang.ac.kr (C. Lee).

1359-6454/$36.00
http://dx.doi.org/10.1016/j.actamat.2012.03.001

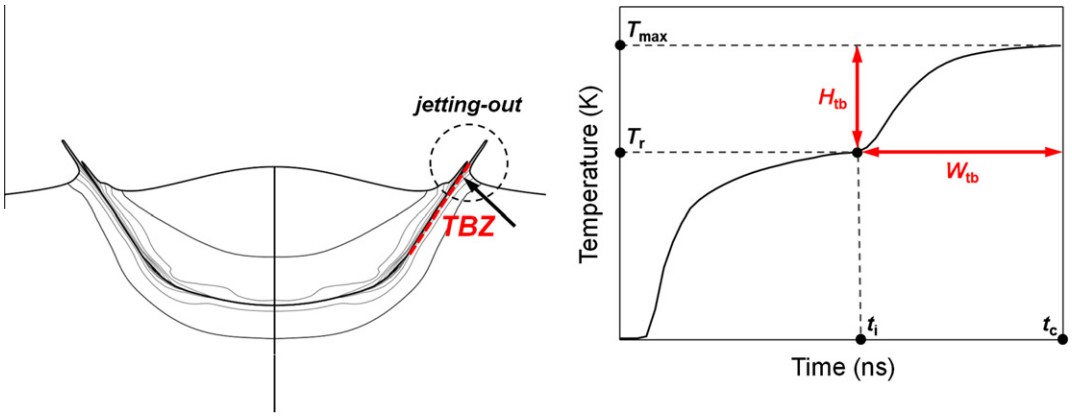

Fig. 1. Schematic representations of a TBZ defined at the localized interface (red dotted line indicated by an arrow) that experiences the abnormal "thermal run-away" phenomenon induced by ASI (as depicted on the right-hand side of the figure) with the occurrence of jetting-out (as marked by a dotted circle) (for details, see Ref. [3]). (For interpretation of the references to color in this figure legend, the reader is referred to the web version of this article.)

Note that, here, the local interfacial region at which the TBZ occurs is also denoted by "TBZ".

Moreover, physico-chemical particle/substrate interactions for dissimilar materials appear as interfacial roll-ups and vortices (i.e., mechanical interlocking) [5], interfacial melting [3,6–9] and rebound phenomena [10–12], which have an effect on the initiation of coating build-up. In previous studies, kinetic spraying of commercially pure Ni (<45 μm particle size) on Al [13], carbon steel [14] and mild steel [15] substrates (using helium (He), nitrogen (N_2) and air as the process gas, respectively) resulted in very thick (~150–300 μm) and dense coatings. Nevertheless, Papyrin et al. [16] reported that the deposition efficiency (DE) of Ni was relatively low (<50%) even at high velocity (~800 m s^{-1}) compared with that of other face centered cubic metals (e.g., Cu and Al). It has also been reported that the DE of Ni coatings with a mean particle size (D_{mp}) of 35 μm on 6061-Al and Cu substrates were <50%, even though He was used as the process gas [8]. In a recent study, it was proposed that the optimum particle size (at a particle impact temperature of 573 K) for enhanced deposition of Ni using N_2 process gas was 35 μm in terms of adhesion and rebound factors estimated by FEM based on the effect of the particle size (for details, see Ref. [17]). Kuroda et al. [18] reported that preheating of metallic powder particles at an optimum temperature (using N_2-diluted combustion gases in a warm spraying process) was quite effective for both densification (with low oxygen content, e.g., minimum value 0.22 mass% in the case of Ti) and grain refinement of kinetic sprayed coatings. In a previous study, Yokoyama et al. [19] also showed by FEM that the critical velocity of Cu decreased significantly with increasing particle impact temperature. Nevertheless, a systematic experimental study (combined with FEM) of the effects of an elevated particle impact temperature on the deposition characteristics, microstructure and properties of kinetic sprayed Ni is currently lacking in the literature.

An increase in DE (~90%) of a Ni coating on a mild steel substrate using N_2 process gas with an enhanced powder preheating system was reported previously [17]. This novel process appears to merit further research and development, because the process operates under an inert environment (directly related to lower oxygen content in the coating) compared with the warm spraying process [4,18]. In the present study, the effects of particle impact conditions (i.e., velocity and temperature) on adhesive (dissimilar) and cohesive (similar) bond formation were investigated by experiments coupled with FEM. The coating could be successfully formed and densified (with less porosity) at a specific particle impact temperature, even below a critical velocity (required at room temperature (RT)) with few particle rebounds. Moreover, the strategy of this thermally associated process optimization was to reduce the process and material costs and effectively achieve improved coating properties (e.g., microhardness and bond strength).

The formation of nanocrystals (NC) (~30–100 nm) in the vicinity of the bonded interfaces in the coating, which improves mechanical properties (e.g., high yield and fracture strengths) [13,20–23], was expected to be tailored by controlling the particle impact conditions, as observed by transmission electron microscopy (TEM) and nanoindentation tests. Hence, the numerical and experimental studies discussed herein will provide a comprehensive understanding of the processing–structure–property relationships in the development of novel kinetic sprayed bulk (thick and dense) Ni for engineering applications, such as near net shape forming and the rapid production of free-standing components [24,25].

2. Experimental procedure

A well-sieved, commercially pure Ni powder (99.5 wt.% purity, Metco 56F-NS and 56C-NS, SULZER METCO) with a nearly spherical or spheroidal morphology (primary

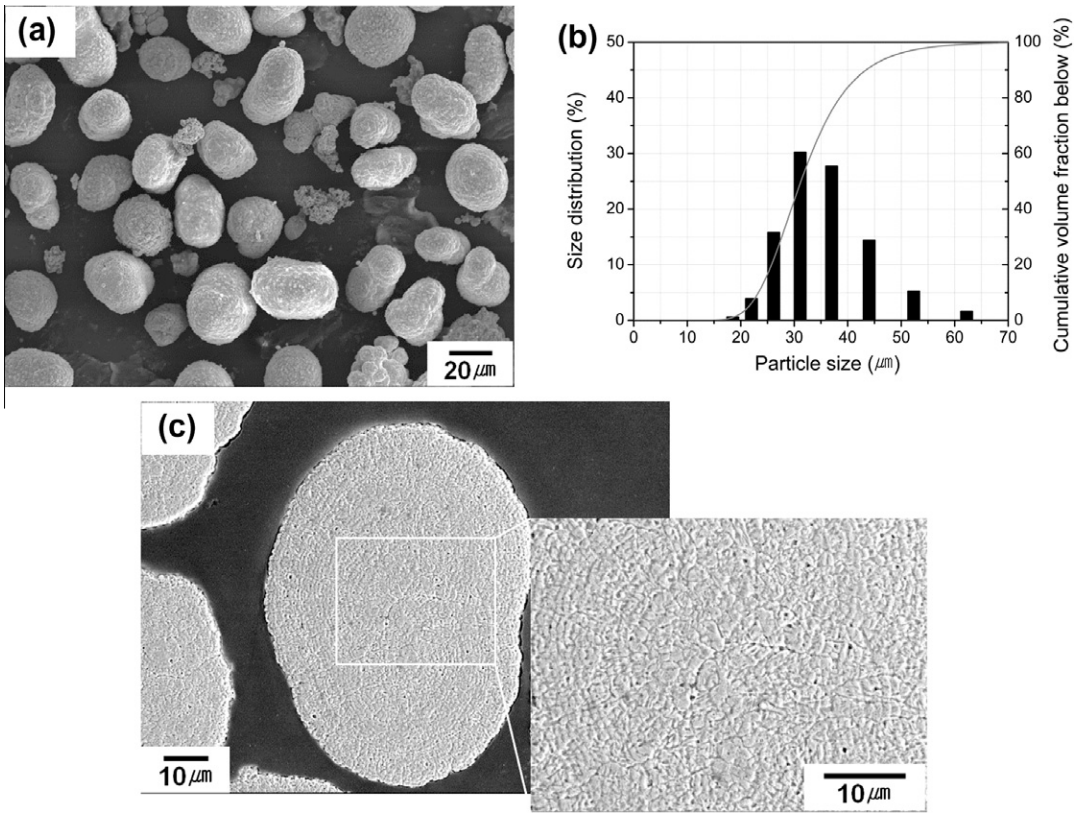

Fig. 2. (a) FE-SEM micrograph of as-sieved powder, "Feedstock 1"; (b) particle size distribution of the feedstock (columns indicate size distribution); and (c) cross-sectional etched micrograph of the powder.

size distribution 26–44 μm ($D_{20} = 26$ μm, $D_{50} = 31$ μm and $D_{90} = 44$ μm)), denoted as "Feedstock 1" (Fig. 2), was deposited onto grit-blasted mild steel substrates using a kinetic spraying system (KINETIC 3000, CGT, Germany) with a powder preheating system [17,26]. The powder was produced by precipitation and aggregation using a hydrogen reduction method and had a mostly dense microstructure (Fig. 2c), although a small number of pores were observed inside and at particle edge from the cross-sectional micrographs of some particles [17]. The particle temperature can reach the preheating temperature regardless of the particle size (typically 25–75 μm) and the process gas temperature, as a result of sufficient heat-up of the particles passing through the elongated coil tube (~6.92 m in length) in the preheater (under N_2 shroud gas environment) attached separately to the kinetic spraying system [26].

A number of spray-coating experiments were performed using N_2 process gas (C_1), N_2 process gas with powder preheating (C_2) and He process gas (C_3), as shown in Table 1. The spray gun was passed over the substrate area three times. Detailed spraying conditions and parameters were described previously [17]. In addition, more finely sieved Ni powder with a D_{mp} of 35 μm (according to a previous study [17]), denoted by "Feedstock 2" (inset in Fig. 9a), was used for spraying experiments as a confirmation run. In this run, N_2 was used as the process gas under the same spraying conditions as those used for "Feedstock 1" and with different powder preheating temperatures, as shown in Table 2.

Table 1
Kinetic spraying process parameters (for "Feedstock 1").

Process conditions	Process gas type	Gas temperature (°C)	Gas pressure (MPa)	Powder preheating temperature (°C)
C_1	N_2	600	2.5	–
C_2	N_2	600	2.5	600
C_3	He	600	1.5	–

Table 2
Kinetic spraying process parameters (for "Feedstock 2").

Process conditions	Process gas type	Gas temperature (°C)	Gas pressure (MPa)	Powder preheating temperature (°C)
$N_{P\text{-}300}$	N_2	600	2.5	300
$N_{P\text{-}400}$				400
$N_{P\text{-}500}$				500
$N_{P\text{-}600}$				600

The DE of the coatings were estimated by calculating the weight fraction of the deposited coatings divided by the total powder used. In order to examine the microstructure of the coatings, cross-sections were taken perpendicular to the coating/substrate interface and polished to a 0.3 μm alumina finish. Some of the specimens were electrochemically

etched using a solution of 25 ml HNO_3 and 75 ml CH_3OH at 6 V for 5 s. A fractured coating surface was obtained by bending the sample. The cross-sectional microstructures and surface morphologies of the powder, coatings and fracture surfaces were observed using scanning electron microscopy (SEM) (JSM-6300, JEOL, Japan) and field emission scanning electron microscopy (FE-SEM) (JSM-6330F, JEOL, Japan).

The Vickers hardness and bond strength of the coatings were measured using a microhardness tester (HMV-2, SHIMADZU, Japan) and a Romulus Bond Strength Tester (QUAD GROUP, USA), respectively, according to test methods and conditions previously described [4,17].

The plane-view thin foils inside the coating (near the substrate), which exhibited the best properties, were prepared by mechanical polishing (up to ~30 μm), followed by electro-polishing using a twin-jet technique in a solution of 10% $HClO_4$ and 90% CH_3CH_2OH at a temperature below −30 °C and ~7 V. The TEM investigations were performed using a field emission transmission electron microscopy (FE-TEM) (JEM-2100F, JEOL, Japan) instrument operating at 200 kV.

Based on the results of the TEM investigations, nanoindentation experiments were performed on the cross-section of the optimized coating to determine the nanostructure (e.g., NC–Ni) using a Nanoindenter-XP (Agilent, Oak Ridge, TN, USA) with a Berkovich indenter [27] under a constant strain rate of 0.05 s^{-1}, a hold time of 1 s and a depth limit of 100 nm. Prior to the tests, the cross-sectional surface was mechanochemically polished to a 0.05 μm colloidal silica suspension finish in order to remove the strain hardened layer induced by mechanical polishing. A total of 400 indentation tests (matrices of 20 × 20 indents) were conducted with an indent spacing of 5 μm.

3. FEM and simulations

A non-linear transient FEM of the high-velocity micron-sized single particle impact (with different particle impact velocities and temperatures) was performed using a commercial explicit code, ABAQUS/Explicit 6.7–2 [28]. The impact velocities of the particles for different spray conditions (Table 1) were estimated with an empirical equation [29]. In a previous study, the fluid dynamic computations revealed that the temperature of Al particles (1–50 μm) at the nozzle exit was <400 K [30]. (Note that the thermal conductivity of Ni is relatively much less than that of Al or Cu: 60.7, 210 and 385 W m^{-1} K^{-1} for Ni, Al and Cu, respectively.) As mentioned in Section 2, the particle temperature after powder preheating could be nearly close to the preheating temperature. The effect of substrate heating by the process gas can be negligible [30]. Accordingly, the initial temperatures of the substrate, C_1 and C_3 particles were assumed to be RT (298 K), while that of the C_2 particle was assumed to be 873 K. The two impact cases, Ni particle onto a mild steel substrate and Ni particle onto a Ni substrate (previously deposited layer), were simulated with a fixed D_{mp} of 35 μm under different particle impact conditions (Table 1). For the latter case, the initial temperatures of the particle and substrate were assumed to be identical. The detailed model construction, boundary conditions, constitutive equations and general/high-strain-rate material properties of the Ni and mild steel were reported previously [3,17].

4. Results and discussion

4.1. Deposition characteristics of Ni particles under different process conditions

Fig. 3a–c shows the cross-sectional polished SEM images of the as-sprayed coatings under different process conditions (Table 1). The DE of the coatings were ~0.5% (almost no weight gain, as shown in Fig. 3a), ~90% and ~20%, for C_1, C_2 and C_3, respectively. Different DE results were obtained with an increase in particle impact velocity and temperature compared with a previous case (for pure Ti [4]), despite the same spraying process parameters. As shown in Fig. 3d–f, a particle detached from the substrate, a particle well-bonded to the previously deposited layer and a severely penetrated and eroded top layer surface (as marked by arrows) were evident for each condition (C_1, C_2 and C_3). The corresponding SEM surface morphologies of the coatings are shown in Fig. 4a–c. Mechanically trapped particles on the roughened substrate, thermally softened, well-deformed particles and highly flattened particles (Fig. 4d–f) were consistent with observations from the cross-sectional images of the coatings (Fig. 3d–f). The thicknesses of the resulting coatings under conditions C_2 and C_3 were ~600 μm and ~120 μm, respectively, and the coatings were both quite dense. The DE of the sample prepared according to C_2 was considerably greater than that in previous cases [13–16], and this difference was attributed to the enhanced thermal softening of the particles [4,31] resulting from powder preheating. In particular, Ni has a relatively high value for thermal softening sensitivity at high strain rates (parameter m based on the Johnson–Cook plasticity model) compared with other materials, such as Cu, Al and Ti [3]. Interestingly, the DE of the C_3 coating was much lower than that of the C_2 coating, despite its dense microstructure. As shown in Figs. 3f and 4f, most of the highly flattened particles seemed to have rebounded [10,11] and/or eroded [2] owing to the large amount of kinetic energy. This feature was evident from the increased microhardness of the C_3 coating (~313 $HV_{0.1}$) compared with that of the C_2 coating (~275 $HV_{0.1}$), owing to the enhanced strain hardening and densification attributed to the tamping effect of high-velocity impacted and rebounded particles [17].

Fig. 5 presents the estimated velocities of the different sized Ni particles under different process conditions (C_1, C_2 and C_3). The zone marked by a dotted rectangle indicates the primary size range of the powder used in the experiments. The critical velocity for a 25 μm Ni particle

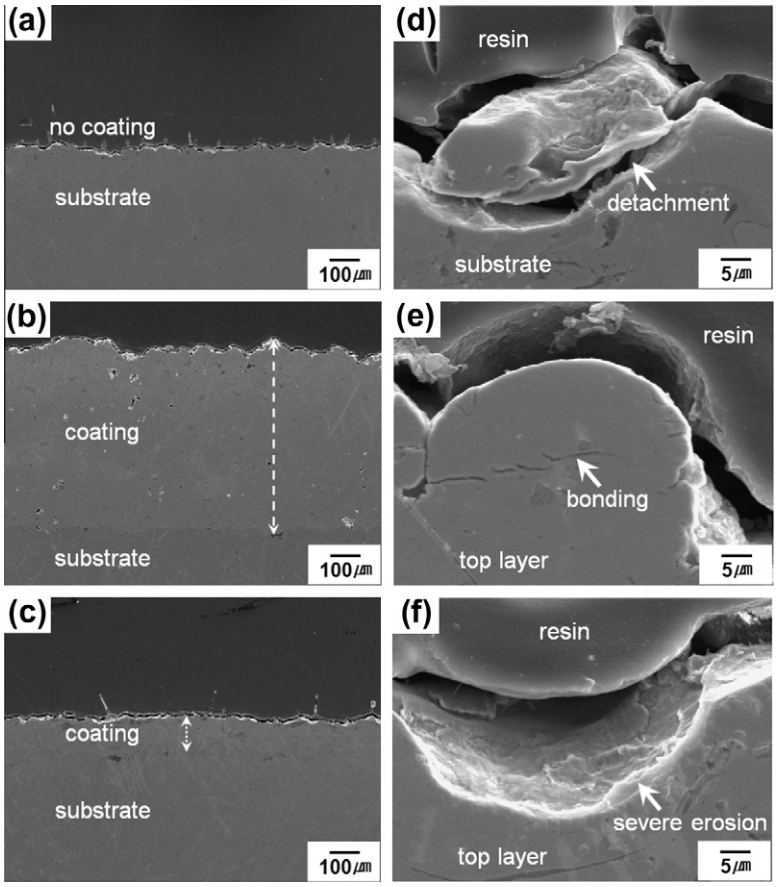

Fig. 3. Cross-sectional SEM micrographs of the coatings for (a) C_1, (b) C_2 and (c) C_3 process conditions; (d)–(f) higher magnifications of the top areas in (a)–(c).

deposition at RT is ~600–700 m s^{-1} [1–3,17,32]. However, the critical velocity for Ni particle deposition onto a mild steel substrate has not yet been reported. The velocity at which the saturation limit of interface temperature occurs with the ASI ($>0.95T_m$) was defined as the theoretical "critical velocity" to confirm the firmly bonded state (i.e., metallurgical bonding) [3]. Note that this criterion (i.e., the definition of "critical velocity") differs from that by Schmidt et al. [32] and Assadi et al. [33] (i.e., 50% DE). This is the reason why there is a discrepancy between the critical velocities reported in the literature [1–3,32]. Although the estimated velocities for the particles for C_1 were always greater than the critical velocities for cohesive bonding (except for 25 μm) [17], the velocities were probably less than the critical velocities for adhesive bonding (i.e., first layer formation) and therefore most of the impacted particles bounced off, as shown in Fig. 4a. Based on the experimental observations (Figs. 3c and 4c), the estimated velocities of the particles for C_3 appeared to be much greater than the critical velocities, because the DE (~20%) did not reach the maximum value, mainly because of the rebounding of the impacted particles. As demonstrated in Ref. [32], the "bounce-off" occurs with low DE (<50%) when the particle velocity is much less than the critical velocity, while the "rebound" occurs after reaching the maximum DE (~100%) owing to excessive kinetic energy. Further increase in particle velocity results in a steep decrease in DE due to the effect of "erosion". Schmidt et al. [2] estimated the erosion velocity of a 25 μm Ni particle (when the DE equals zero over the critical velocity) to be ~1250 m s^{-1}. As a result, "Feedstock 1" (with a D_{mp} of ~30 μm) might have a relatively lower erosion velocity according to the effect of the particle size [2,17]. Hence, adequate critical velocities seemed to exist between the two velocities for C_1 and C_3, as depicted by a solid line, $v_{cr,RT}$, in Fig. 5. As schematically shown by the dotted line, $v_{cr,PH}$, the critical velocities for both adhesive and cohesive bonding could be effectively decreased by powder preheating to allow for the increase in DE shown in Fig. 3b. The above-mentioned deposition characteristics will be discussed further based on the FEM results in the following sections.

4.2. Effect of particle impact conditions on adhesive and cohesive bonding

Fig. 6a–c shows the equivalent von Mises flow stress profiles (at CPRESS = 0) generated by FEM for a 35 μm Ni particle impact onto a mild steel substrate under different process conditions (C_1, C_2 and C_3) where CPRESS [26]

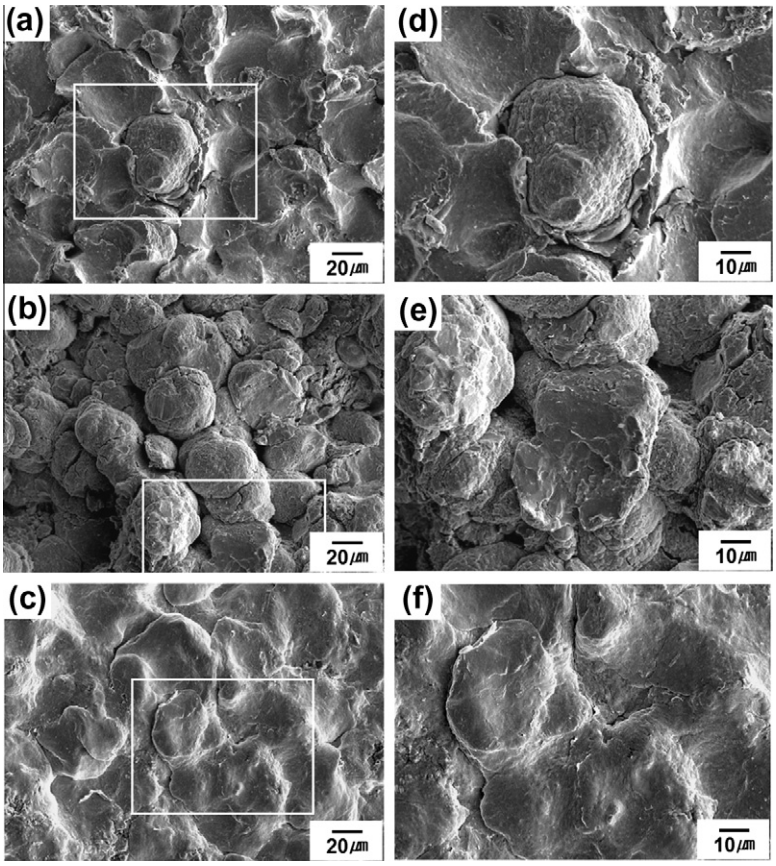

Fig. 4. FE-SEM surface morphologies of as-sprayed coatings for (a) C_1, (b) C_2 and (c) C_3 process conditions; (d)–(f) higher magnifications of the boxed areas in (a)–(c).

indicates the contact pressure at the interface. The maximum stress value for C_2 appeared to be significantly lower (893.6 MPa) than that for C_1 or C_3 (914.8 MPa and 913.6 MPa, respectively). Additionally, the region in which stress propagated inside the substrate for C_2 was considerably narrower, implying that a less repulsive wave was generated during unloading compared with C_1 and C_3.

As shown in the left-hand side of Fig. 6d (magnifications of Fig. 6a–c), the stress distribution of a highly strained

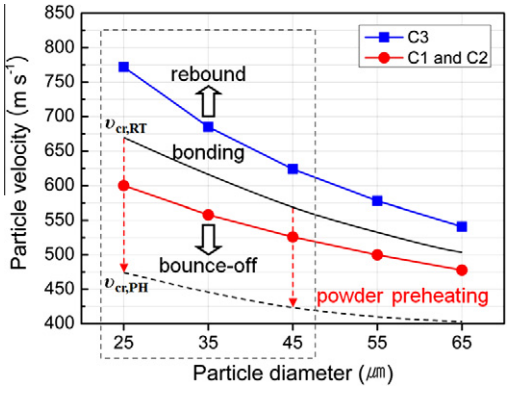

Fig. 5. Estimated velocities of different sized Ni particles for different process conditions (C_1, C_2 and C_3) combined with a schematic showing the critical velocities; $v_{cr,RT}$ (solid line) and $v_{cr,PH}$ (dotted line) indicate the critical velocities without and with powder preheating, respectively.

particle and substrate for each condition was quite distinguishable. The labels 'a' and 'b' in the figure indicate the regions at which maximum stress values were observed within the particle and substrate, respectively. Notably, the stress value of the deformed particle for C_2 was markedly lower (599.6 MPa) than that for C_1 or C_3 (914.8 MPa and 908.8 MPa, respectively), mainly owing to the effect of thermal softening enhanced by powder preheating. The right-hand side of Fig. 6d shows that the maximum temperature evolved in the TBZ for C_2 was the greater (1372 K) than that for C_1 or C_3 (983.7 K and 1052 K, respectively). The effect of powder preheating revealed a similar tendency compared with the FEM results for the Cu–carbon steel combination previously reported by Yokoyama et al. [19]. Note that these values were obtained before approximation using linear extrapolation to the zero element size [1,17].

The combination of Ni and mild steel had a relatively higher effective elastic modulus $(1/E^* = (1-\nu_1^2)/E_1 + (1-\nu_2^2)/E_2$ [34], where ν_1, ν_2, E_1 and E_2 are the Poisson's ratio and elastic modulus of the particle and substrate, respectively), compared with that of other dissimilar combinations [3]. The higher the effective elastic modulus, the lower the recoil coefficient (i.e., rebound energy) [10,11]. Nevertheless, the Ni has a higher strain hardening exponent (parameter n) and modulus (coefficient B) relative to

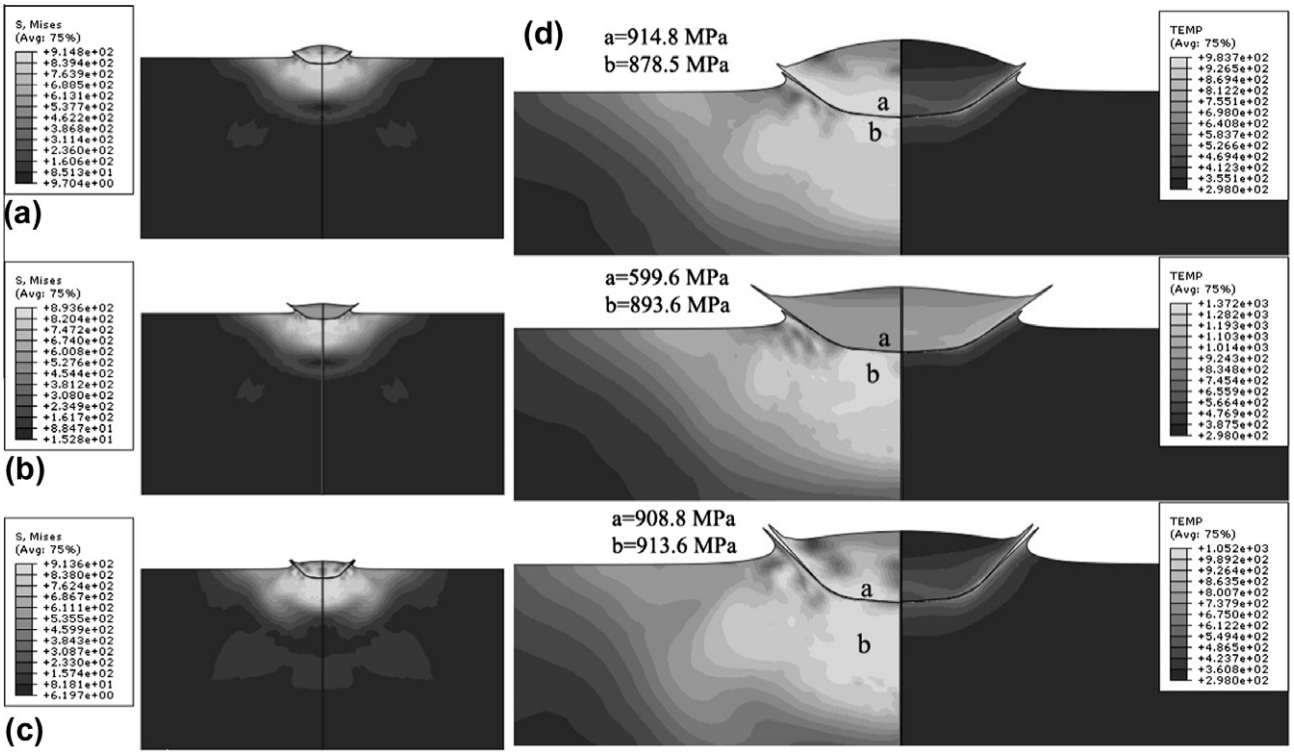

Fig. 6. Finite-element simulations of a 35 μm Ni particle impact onto a mild steel substrate: equivalent von Mises flow stress profiles at CPRESS = 0 for (a) C_1, (b) C_2 and (c) C_3 process conditions; (d) magnifications of (a)–(c) (left-hand side) and the corresponding temperature profiles (right-hand side).

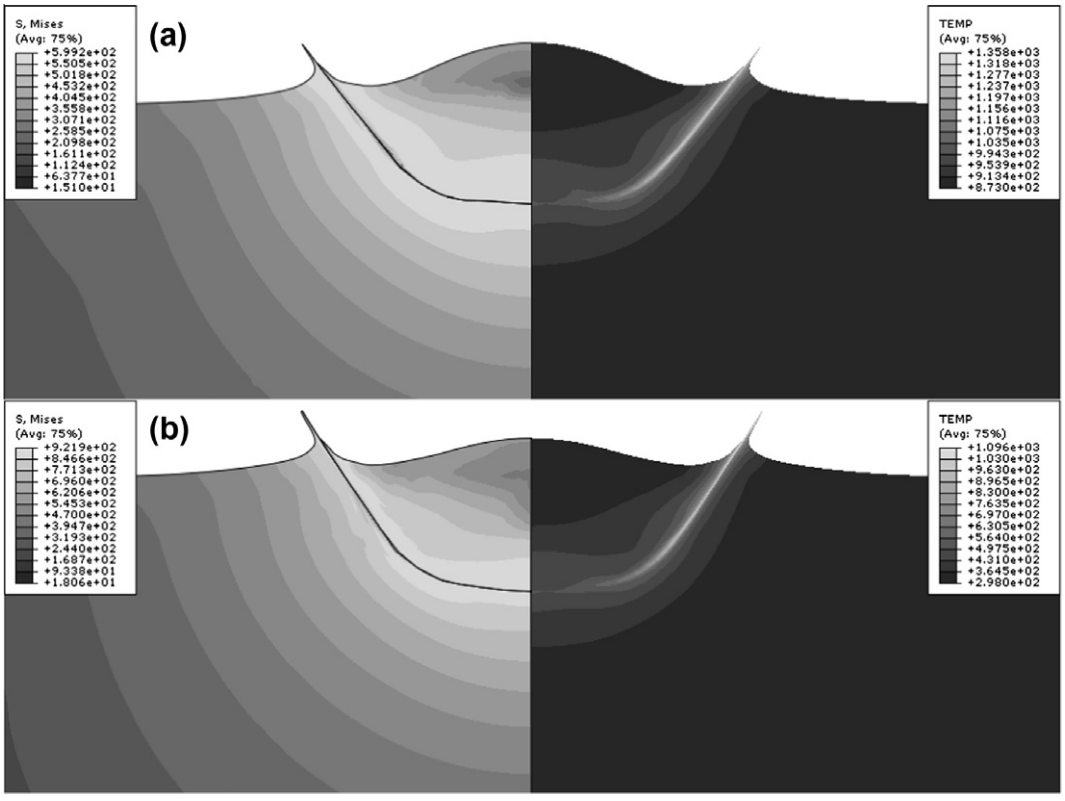

Fig. 7. Finite-element simulations of a 35 μm Ni particle impact onto a Ni substrate: equivalent von Mises flow stress profiles (left-hand side) and the corresponding temperature profiles (right-hand side) at 60 ns for (a) C_2 and (b) C_3 process conditions.

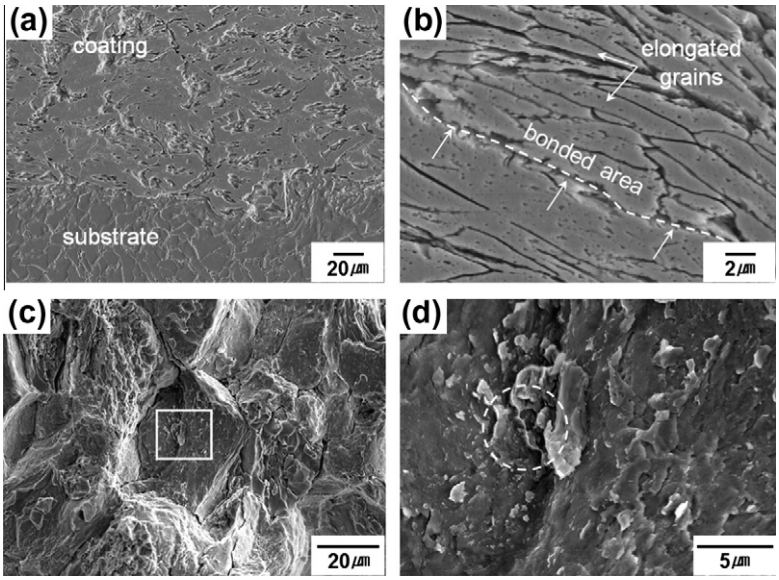

Fig. 8. Ni coating for the C_2 process condition: (a) cross-sectional etched FE-SEM micrograph; (b) high-magnification of a well-bonded area in the coating; (c) FE-SEM fractured surface morphology of the coating; and (d) higher magnification of the boxed area in (c).

that of Cu, Al and Ti, despite its greater thermal softening exponent (parameter m) at high strain rates [3]. Additionally, mild steel has a much higher yield stress (532 MPa) than that of Ni (163 MPa) [3]. Hence, the combined effects of these specific physico-mechanical properties and the high-strain-rate thermomechanical characteristics enhanced the "bounce-off" of impacting particles, which resulted in the failed formation of the first layer, as shown in the previous section (Figs. 3a and 4a).

In the case of C_2 (with powder preheating), however, as suggested by Wu et al. [10], the rebound energy of the impacting bodies ($R = 3.0\left(\overline{\sigma}_Y^{\frac{5}{4}}/E^*\right) d_p^3 \rho_p^{\frac{3}{4}} v_p^{\frac{3}{2}}$, where d_p, ρ_p, v_p and $\overline{\sigma}_Y$ are the size, density and velocity of the particle, and effective yield stress of the particle and substrate during impact, respectively) was significantly decreased owing to the decrease in $\overline{\sigma}_Y$ (based on the Johnson–Cook plasticity model [1–4,11]) by dominant thermal softening compared with strain hardening. Moreover, the pronounced "jetting-out phenomenon" due to the enhanced ASI and the increased flattening of the deformed particle most likely resulted in the strengthened adhesive bonds by increasing the interface temperature and removing most of the oxides on the particle and substrate surfaces [35,36]. Note that the estimated flattening ratios (defined as $1 - D/d_p$, where D and d_p are the diameter of the deformed particle and the initial particle, respectively) for C_1, C_2 and C_3 were 0.49, 0.59 and 0.52, respectively.

In spite of the considerably higher flow stress (showing slight separation at the jetting-out region) for C_3, adhesive bonding was triggered because of the enhanced interface temperature and flattening of the deformed particle, which are beneficial for both metallurgical bonding and mechanical interlocking.

Fig. 7 shows the equivalent von Mises flow stress (left-hand side) and corresponding temperature (right-hand side) profiles (at 60 ns) determined by FEM for the 35 μm Ni particle impact onto a Ni substrate (previously deposited layer) under different process conditions (C_2 and C_3). Note that the simulations here were performed only up to 60 ns (showing successful outputs) to acquire more reliable results by avoiding the element failure that results in severe distortion error during computations [17]. Although this simple model did not reflect the real impact conditions (i.e., particle-to-particle [4,23]), the maximum stress in C_2 was much lower (599.2 MPa), and the maximum temperature evolved at the localized interface (i.e., TBZ with a light grey contrast) was significantly greater (1358 K) than that for C_3 (921.9 MPa and 1096 K, respectively). Accordingly, these FEM results corroborated the noticeably increased DE of the C_2 coating compared with the C_3 coating shown in the previous section (Fig. 3b and c).

Fig. 8a shows a SEM micrograph of an etched cross-section of a C_2 coating close to the coating/substrate interface. According to the previously mentioned effects, very intimate particle–substrate and particle–particle bonding was clearly observed. High magnification of another region of the coating (Fig. 8b) revealed extremely elongated grains in a severely deformed particle and a well-bonded area (interparticle boundary) as marked by arrows (for the detailed microstructure, see Ref. [17]). After the sample had been bent, the fractured surface morphology of the coating (Fig. 8c) was rougher than that of the coating without powder preheating [15]. Notably, the high-magnification of the boxed area in Fig. 8c showed a ruptured surface with weakly developed "dimple" pattern, as indicated by a dotted circle (Fig. 8d), which may suggest a stronger metallurgical bonding between the deposited particles, as reported in earlier studies of Ti [4,15] and Cu [32,37].

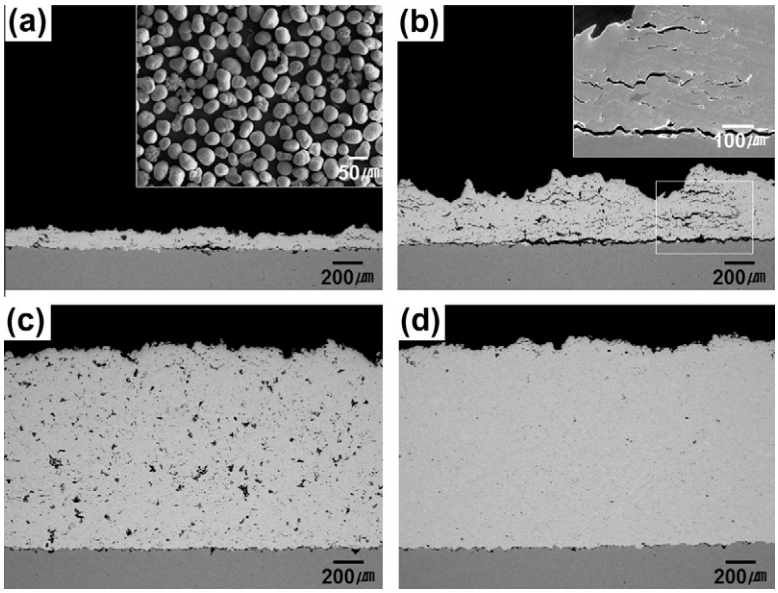

Fig. 9. Cross-sectional SEM micrographs (using BSE mode) of the coatings for process conditions (a) $N_{P\text{-}300}$ (inset shows FE-SEM micrograph of as-sieved powder, "Feedstock 2"), (b) $N_{P\text{-}400}$ (inset shows higher magnification of the boxed area), (c) $N_{P\text{-}500}$ and (d) $N_{P\text{-}600}$.

4.3. Correlation of coating properties with elevated particle impact temperature

Fig. 9 shows the SEM micrographs (backscattered electron (BSE) mode) of the coatings using "Feedstock 2" (inset in Fig. 9a) with an optimum particle size (~35 μm [17]). As the powder preheating temperature increased according to the conditions in Table 2, the DE and coating quality appeared to improve significantly. Fig. 10 shows the coating thickness (plots with a sigmoidal fit) and bond strength (columns) for different powder preheating temperatures. Interestingly, the DE of the coating suddenly increased to ~95% at a preheating temperature of 773 K ($N_{P\text{-}500}$). Despite the considerably higher particle impact velocity than the critical velocities for cohesive bonding [17], the velocity was most likely not sufficient in the cases of lower preheating temperatures (i.e., $N_{P\text{-}300}$ and $N_{P\text{-}400}$) for a successful adhesive (and partially cohesive) bonding as discussed in Section 4.1. The cracks that formed between the particles and particle/substrate (especially shown in the inset in Fig. 9b) corroborated this presumption. Notably, with increasing preheating temperature (up to 873 K, $N_{P\text{-}600}$), the coating appeared to become more dense, and thus had nearly no pores compared with the $N_{P\text{-}500}$ coating with a ~3.3% porosity estimated based on the image analysis method [4,17]. Accordingly, the microhardness of the $N_{P\text{-}600}$ coating (278 ± 15 $HV_{0.1}$) was also slightly greater than that of the $N_{P\text{-}500}$ coating (274 ± 19 $HV_{0.1}$). As shown in Fig. 10, the bond strength of the $N_{P\text{-}600}$ coating (68 ± 3 MPa) was much greater than that of the $N_{P\text{-}500}$ coating (53 ± 6 MPa), which was also greater than the previous case (using "Feedstock 1" denoted by S_1 in Ref. [17]). The failure modes of the coatings were both cohesive, implying that the adhesive strengths were greater than the cohesive strengths of the coatings. Consequently, these experimental results corroborated the FEM results in Section 4.2 (see Figs. 6 and 7).

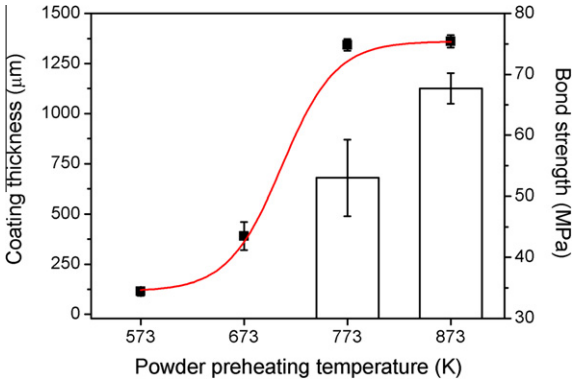

Fig. 10. Coating thickness and bond strength for different powder preheating temperatures (columns indicate bond strength).

The notably improved properties (i.e., DE, microhardness and especially the bond strength) of the $N_{P\text{-}600}$ coating could be explained by the well-established theory of TBZ enhanced by thermally accelerated ASI [3,4]. Fig. 11a shows the temporal evolution of the interface temperature for Ni particle deposition determined by FEM at a fixed particle impact velocity of 640 m s^{-1} (below the critical velocity at RT [3,17]) for different particle impact temperatures; note that a 25-μm particle size was chosen as a general reference model [2,3]). The thermally accelerated ASI was most pronounced at a particle impact temperature of 773 K, which led to a maximum interface temperature of $0.99T_m$ (nearly saturated). This was mainly because of a decrease in the critical shear strain for instability ($\gamma_c = n\rho c/0.9(\partial\tau/\partial T)$ [38], where n, ρ, c and $\partial\tau/\partial T$ are the strain hardening exponent, density, heat capacity and derivative of shear strength with respect to the temperature, respectively). Owing to the effect

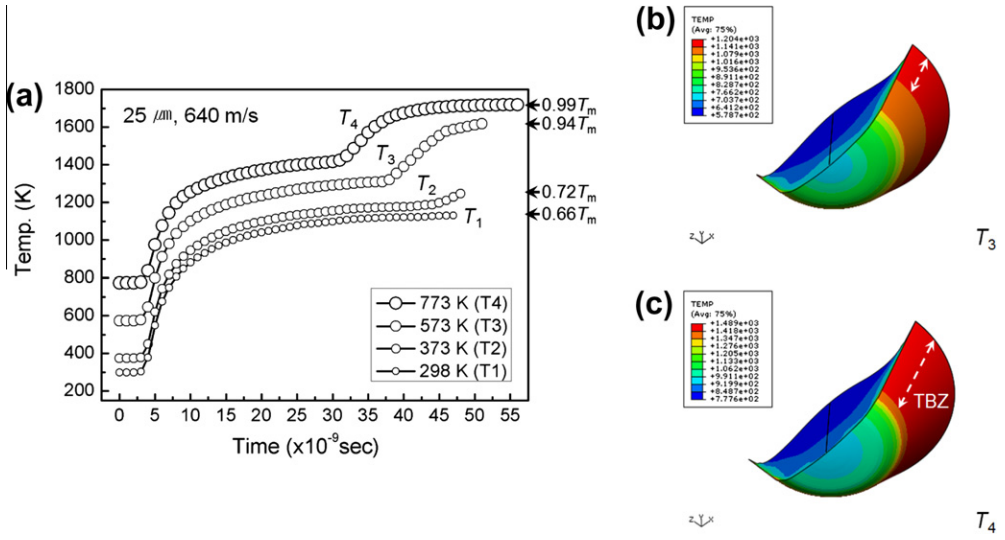

Fig. 11. Finite-element simulations of Ni particle deposition for a 25 μm particle at 640 m s^{-1}: (a) temporal evolution of interface temperature for different particle impact temperatures and the corresponding interface temperature profiles of (b) T_3 and (c) T_4; the regions in red indicate the TBZ.

of powder preheating [4,26,31], the rate of thermal softening ($\partial\tau/\partial T$) increased, resulting in a decrease in the critical strain for ASI. Hence, the TBZ (indicative of a well-bonded region) [3,4] attributed to strain-induced adiabatic heating of the deformed particle increased, as shown in Fig. 11b and c.

The activation energy of the chemical bonds (E_a) for Ni was ~1.5–3.0 times greater than that of other metals (e.g., Al, Cu and Ti) [39], which might result in the relatively low DE of the Ni coatings [8,15,16]. Nevertheless, the enhanced adhesion factors (such as interface temperature, contact area and contact time) [4,17] resulting from the thermally accelerated ASI may compensate for or overcome E_a in terms of the adhesion energy [10,11].

4.4. Nanocrystal formation enhanced by power preheating

In this section, the NC structure formed in the $N_{P\text{-}600}$ coating (Fig. 9d) is introduced by investigating the results of TEM observations together with nanoindentation assessments and comparing them with those previously reported in the literature.

It was recently reported by Zou et al. [40] that the Ni coating formed with smaller particles (<25 μm in diameter) using N_2 process gas without powder preheating had ultrafine crystals (UFC) with a grain size of 100–200 nm with high angle boundaries only near the bonded particle interfaces, as characterized by electron backscattered diffraction. In an earlier study, using TEM, Borchers et al. [41] also observed UFC with a slightly oblong morphology and grain sizes of 100–300 nm at the regions close to the interparticle boundaries in a similar Ni coating. Both groups elucidated these microstructural features using the model of rotational dynamic recrystallization (RDR) proposed by Meyers et al. [42].

Fig. 12 shows a representative high-magnification bright-field TEM micrograph (most probably) near the bonded interface (i.e., TBZ) in the $N_{P\text{-}600}$ coating. The region denoted by a dotted line in the figure (near a hole) is inferred to be interparticle boundaries, because they can be preferential etching sites [41]; many regions near the holes in the samples revealed a similar microstructure. In comparison with those previously reported [40,41], NC (~30–100 nm) were formed (as marked by black arrows) along with the UFC (>100 nm but < 500 nm), as marked by white solid arrows. A bimodal grain size distribution was prominent (as denoted by a dotted circle), which can also confer both high strength and good ductility of a bulk fine-grained material [43–45]. Based on the RDR mechanism [42], via powder preheating, the activation energy for grain boundary diffusion might be readily supplied during the high-strain-rate deformation, promoting the thermally activated RDR process in a shorter period [46].

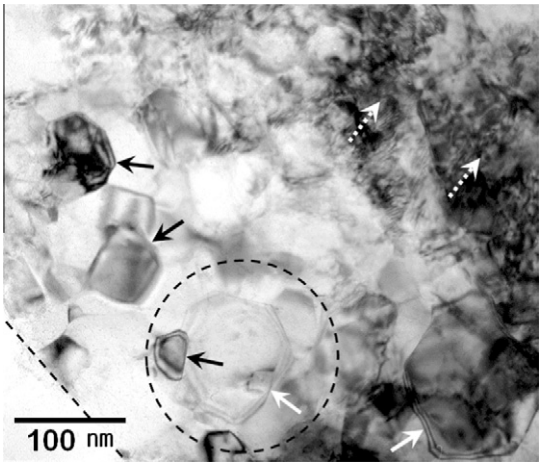

Fig. 12. High-magnification bright-field TEM micrograph near the bonded interface of the $N_{P\text{-}600}$ coating; the region denoted by a dotted line is inferred to be an interparticle boundary.

Note that the preheating temperature for $N_{P\text{-}600}$ was $\sim 0.5T_m$. The similar features of the strain-induced subgrains with high-density dislocations (showing heavy strain contrast, marked by dotted arrows) [47] were also revealed, as previously reported by Borchers et al. [41]. As in the cases of warm spraying [31,35,36], the effect of thermal softening enlarged the strain field of the deformed particle (Figs. 6 and 7), such that the grain refinement process was further enhanced. It is also most probable that the subsequent impact of the heated particles can induce the re-grain refinement of UFC, forming finer NC [35], owing to the effect of strain and heat accumulation [23].

The nanoindentation tests of the coating clearly revealed that the nanohardness values were not homogeneous and varied in the range ~2.7–5.5 GPa (see the typical load–displacement (P–h) curves in Fig. 13), which were similar to the results reported by Zou et al. [48]. The inhomogeneity of the nanohardness values, influenced by the combined effects of grain boundary and dislocation density, reflects the microstructural features observed in the coating (i.e., necklace-like structure [48]). As a result, the overall microhardness of the coating was much lower ($278 \pm 15\ HV_{0.1}$) than that of the NC-Ni coating ($605 \pm 13\ HV_{0.3}$) [13]. Nevertheless, the maximum nanohardness (~5.5 GPa) was close to the value of the electrodeposited NC-Ni with a mean grain size of ~40 nm (measured at an indentation depth limit of 100 nm) [21]. Additionally, the value nearly reached the values of the NC-Ni with a grain size of 20 nm (5.1–6.0 GPa) [49], although it was less than that of the NC-Ni with a grain size of 6 nm (7.6–9.7 GPa) [50].

Metal NC (usually < 100 nm) are responsible for the high strength and low-temperature superplasticity (at $0.36T_m$ for the NC-Ni [51]) attributed to the Hall–Petch relation and the grain boundary sliding mechanism [22,23,51,52]. Hence, the UFC zone formed with the NC near the TBZ (i.e., bonded zone) would be beneficial in enhancing the fracture strength of the deposits, as evidenced by the transparticle ductile dimple rupture shown in earlier studies [4,23]. However, these characteristics were not observed here, which might be due to the insufficient interparticle bond strength (68 ± 3 MPa). Hence, further optimization of the deposition process is required by tailoring the particle impact conditions, and this is being addressed in ongoing efforts to achieve low-temperature and high-strain-rate ($>10^{-2}\ s^{-1}$) superplasticity [51,53] of kinetic sprayed bulk Ni.

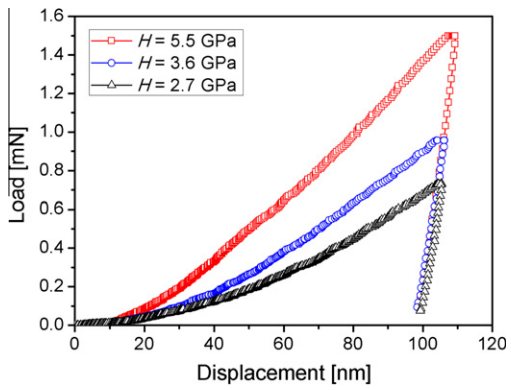

Fig. 13. Typical nanoindentation P–h curves for the $N_{P\text{-}600}$ coating.

5. Conclusions

In the present study, the correlation of particle impact conditions with bonding, microstructure and mechanical properties in kinetic spraying of Ni particles onto a mild steel substrate were investigated through numerical and experimental approaches. The following conclusions were drawn.

1. Owing to the effect of thermal softening, the DE of Ni was more improved (>95%) with powder preheating than with higher particle impact velocity at RT. FEM results indicated that higher particle impact temperature (up to 873 K) was responsible for enhanced adhesive and cohesive bonding, owing to the suppression of the equivalent (von Mises) flow stress and increase in strain-induced interface heat-up of the impacting bodies.
2. The coating was successfully formed and densified (with less porosity) at a specific particle impact temperature (i.e., powder preheating $\sim 0.5T_m$), even below a critical velocity (required at RT). The microhardness and bond strength of the coating were greatly enhanced ($278 \pm 15\ HV_{0.1}$ and 68 ± 3 MPa, respectively) compared with lower particle impact temperatures. The notably improved properties (i.e., DE, microhardness and bond strength) of the coating were attributed to the TBZ (indicative of a well-bonded area) enhanced by thermally accelerated ASI.
3. The formation of NC (~30–100 nm) in the vicinity of the bonded interfaces, which would be beneficial for high yield and fracture strengths of deposits, was enhanced due to the effects of thermal activation and softening (at $\sim 0.5T_m$) and additional straining of the deformed particles. This warrants further investigation to optimize the deposition process and tailor the microstructure (processes which are quite challenging) in order to achieve the low-temperature and high-strain-rate superplasticity of kinetic sprayed bulk Ni, as was previously observed in the electrodeposited NC-Ni.

Acknowledgement

This work was supported by a grant from the National Research Foundation of Korea (NRF) funded by the Korean government (MEST) (No. 2011-0016724).

References

[1] Assadi H, Gärtner F, Stoltenhoff T, Kreye H. Acta Mater 2003;51:4379.
[2] Schmidt T, Gärtner F, Assadi H, Kreye H. Acta Mater 2006;54:729.
[3] Bae G, Xiong Y, Kumar S, Kang K, Lee C. Acta Mater 2008;56:4858.
[4] Bae G, Kumar S, Yoon S, Kang K, Na H, Kim HJ, et al. Acta Mater 2009;57:5654.
[5] Grujicic M, Saylor JR, Beasley DE, DeRosset WS, Helfritch D. Appl Surf Sci 2003;219:211.
[6] King PC, Zahiri SH, Jahedi M. Acta Mater 2008;56:5617.
[7] King PC, Bae G, Zahiri SH, Jahedi M, Lee C. J Therm Spray Technol 2010;19(3):620.
[8] Xiong Y, Bae G, Xiong X, Lee C. J Therm Spray Technol 2010;19(3):575.
[9] Xiong Y, Xiong X, Yoon S, Bae G, Lee C. J Therm Spray Technol 2011;20(4):860.
[10] Wu J, Fang H, Yoon S, Kim H-J, Lee C. Scripta Mater 2006;54:665.
[11] Ji Y, Bae G, Kang K, Lee C. Metal Mater Int 2011;17(2):335.
[12] Kim KH, Watanabe M, Mitsuishi K, Iakoubovskii K, Kuroda S. J Phys D – Appl Phys 2009;42:065304.
[13] Ajdelsztajn L, Jodoin B, Schoenung JM. Surf Coat Technol 2006;201:1166.
[14] Koivuluoto H, Lagerbom J, Vuoristo P. J Therm Spray Technol 2007;16(4):488.
[15] Li W-Y, Zhang C, Guo X, Li C-J, Liao H, Coddet C. Appl Surf Sci 2007;254:517.
[16] Papyrin AN, Kosarev VF, Klinkov SV, editors. Cold spray technology. Amsterdam: Elsevier; 2006. p. 25–7.
[17] Bae G, Kang K, Na H, Kim J-J, Lee C. Surf Coat Technol 2010;204:3326.
[18] Kuroda S, Watanabe M, Kim KH, Katanoda H. J Therm Spray Technol 2011;20(4):653.
[19] Yokoyama K, Watanabe M, Kuroda S, Gotoh Y, Schmidt T, Gärtner F. Mater Trans 2006;47(7):1697.
[20] Mishra R, Basu B, Balasubramaniam R. Mater Sci Eng A – Struct 2004;373:370.
[21] Schwaiger R, Moser B, Dao M, Chollacoop N, Suresh S. Acta Mater 2003;51:5159.
[22] Kumar KS, Suresh S, Chisholm MF, Horton JA, Wang P. Acta Mater 2003;51:387.
[23] Bae G, Kang K, Kim J-J, Lee C. Mater Sci Eng A – Struct 2010;527:6313.
[24] King PC, Zahiri SH, Jahedi M. Metall Mater Trans A 2009;40A:2115.
[25] Hussain T, McCartney DG, Shipway PH, Marrocco T. J Therm Spray Technol 2011;20(1–2):260.
[26] Yoon S, Kim H-J, Lee C. Surf Coat Technol 2006;200:6022.
[27] Choi I-C, Yoo B-G, Kim Y-J, Seok M-Y, Wang Y, Jang J-I. Scripta Mater 2011;65:300.
[28] ABAQUSTM 6.7–2 user manual. Pawtucket (RI, USA): Hibbitt, Karlsson and Soerensen; 2007.
[29] Wu J, Fang H, Yoon S, Kim H-J, Lee C. Appl Surf Sci 2005;252:1368.
[30] Kwon EH, Cho SH, Han JW, Lee C, Kim H-J. Metal Mater Int 2005;11(5):377.
[31] Kim KH, Watanabe M, Kuroda S. Scripta Mater 2009;60:710.
[32] Schmidt T, Assadi H, Gärtner F, Richter H, Stoltenhoff T, Kreye H, et al. J Therm Spray Technol 2009;18(5–6):794.
[33] Assadi H, Schmidt T, Richter H, Kliemann J-O, Binder K, Gärtner F, et al. J Therm Spray Technol 2011;20(6):1161.
[34] Johnson KL, editor. Contact mechanics. Cambridge: Cambridge University Press; 1985. p. 92.
[35] Kim KH, Watanabe M, Kuroda S. J Therm Spray Technol 2009;18(4):490.
[36] Kim KH, Watanabe M, Kuroda S. Surf Coat Technol 2010;204:2175.
[37] Schmidt T, Gärtner F, Kreye H. J Therm Spray Technol 2006;15(4):488.
[38] Semiatin SL, Staker MR, Jonas JJ. Acta Metall Mater 1984;32:1347.
[39] Papyrin AN, Klinkov SV, Kosarev VF. In: Marple BR, Moreau C, editors. Thermal spray 2003: advancing the science and applying the technology. Materials Park (OH): ASM International; 2003. p. 27–35.
[40] Zou Y, Qin W, Irissou E, Legoux J-G, Yue S, Szpunar JA. Scripta Mater 2009;61:899.
[41] Borchers C, Gärtner F, Stoltenhoff T, Kreye H. J Appl Phys 2004;96(8):4288.
[42] Meyers MA, Xu YB, Xue Q, Perez-Prado MT, McNelley TR. Acta Mater 2003;51:1307.
[43] Ramtani S, Dirras G, Bui HQ. Mech Mater 2010;42:522.
[44] Zhang X, Wang H, Scattergood RO, Narayan J, Koch CC, Sergueeva AV, et al. Acta Mater 2002;50:4823.
[45] Shen X, Lian J, Jiang Z, Jiang Q. Mater Sci Eng A – Struct 2008;487:410.
[46] Yang Y, Wang BF. Mater Lett 2006;60:2198.
[47] Dudova N, Belyakov A, Sakai T, Kaibyshev R. Acta Mater 2010;58:3624.
[48] Zou Y, Goldbaum D, Szpunar JA, Yue S. Scripta Mater 2010;62:395.
[49] Gu CD, Lian JS, Jiang Q, Zheng WT. J Phys D – Appl Phys 2007;40:7440.
[50] Gu CD, You YH, Yu YL, Qu SX, Tu JP. Surf Coat Technol 2011;205:4928.
[51] McFadden SX, Mishra RS, Valiev RZ, Zhilyaev AP, Mukherjee AK. Nature 1999;398:684.
[52] Tjong SC, Chen H. Mater Sci Eng R 2004;45:1.
[53] Wang YM, Bringa EM, McNaney JM, Victoria M, Caro A, Hodge AM, et al. Appl Phys Lett 2006;88:061917.